

# Over-the-air Multifunctional Wideband Electromagnetic Signal Processing using Dynamic Scattering Arrays

Davide Dardari, *Fellow, IEEE*

**Abstract**—To meet the stringent requirements of next-generation wireless networks, multiple-input multiple-output (MIMO) technology is expected to become massive and pervasive. Unfortunately, this could pose scalability issues in terms of complexity, power consumption, cost, and processing latency. Therefore, novel technologies and design approaches, such as the recently introduced holographic MIMO paradigm, must be investigated to make future networks sustainable. In this context, we investigate the concept of a dynamic scattering array (DSA) as a versatile electromagnetic (EM) structure capable of performing joint wave-based computing and radiation by moving the processing from the digital domain to the EM domain. We provide a general, wideband analytical framework for modeling the DSA, which includes a power matching network and realistic reconfigurable loads. Then we introduce specific design algorithms, and apply them to various use cases. We demonstrate that some recent EM processing structures can be seen as particular cases of our general framework. The examples presented in the numerical results corroborate the potential of DSAs to reduce complexity and the number of radiofrequency (RF) chains in holographic MIMO systems while achieving enhanced EM wave processing and radiation flexibility for tasks such as beamforming and single- and multi-user MIMO, also exhibiting superdirective capabilities.

**Index Terms**—Dynamic Scattering Arrays, Holographic MIMO; EM signal processing; Stacked intelligent metasurfaces; superdirectivity.

## I. INTRODUCTION

NEXT-generation wireless systems are expected to provide enhanced performance in terms of capacity, reduced latency, and new functionalities such as integrated sensing and communication [1], [2]. This trend is driving the investigation of fundamental limits using physically consistent models, new technologies, and novel design paradigms to approach them [3]–[7].

One direction of research is the utilization of high-frequency bands in the millimeter wave and THz ranges, coupled with the integration of extremely large antenna arrays (ELAA) [8], which is expected to open up the potential to utilize the extra degrees-of-freedom (DoF) provided by the channel in the radiating near-field propagation region, even under line-of-sight (LOS) conditions [9]–[14]. However, this is pushing current technology towards insurmountable barriers in hardware complexity and power consumption. This issue, also known

D. Dardari is with the Dipartimento di Ingegneria dell’Energia Elettrica e dell’Informazione “Guglielmo Marconi” (DEI), WiLAB-CNIT, University of Bologna, Cesena Campus, Cesena (FC), Italy, (e-mail: davide.dardari@unibo.it).

as *digital bottleneck*, poses serious challenges for the sustainability of future wireless networks. In MIMO-based systems, hybrid digital-analog solutions have been extensively explored to partially alleviate these issues by reducing the number of radiofrequency (RF) chains and the digital processing burden, albeit at the expense of flexibility [7], [15].

A promising approach toward sustainability is to delegate part of the signal processing directly to the EM level, known as electromagnetic signal and information theory (ESIT) [16]–[19]. This can be achieved by designing reconfigurable EM environments [20] using novel EM metamaterials devices to perform basic processing functions (e.g., spatial first derivative) [21], reconfigurable intelligent surfaces (RISs), or the recently introduced stacked intelligent metasurfaces (SIMs) [22]. More in general, holographic MIMO surfaces are envisioned as an efficient implementation of large antenna systems, advancing beyond massive MIMO and ELAAs using simplified and reconfigurable hardware that is reduced in size, cost and power consumption, and facilitate signal processing in the EM domain [23].

Within this context, an appealing recent solution to realize flexible and compact EM processing structures is given by the dynamic scattering array (DSA) [24], [25]. A DSA can be viewed as a generalization of reactively controlled arrays, initially introduced in [26], and their evolution into electrically steerable passive array radiators (ESPARs) [27] and SIMs, toward the realization of multifunctional wave processing. A DSA comprises a limited number of active antenna elements, each connected to an RF chain (input), and is surrounded by a cluster of many reconfigurable passive scatterers. These scatterers interact within the reactive near field, enabling EM processing and radiation to occur jointly “over the air”, thus offering several advantages with respect to other solutions, as investigated in this paper.

### A. Related State of the Art

The idea of introducing passive scattering elements close to an antenna to exploit mutual coupling in the reactive near-field region and shape its radiation properties dates back to the early days of wireless transmissions. A pioneering work is that by H. Yagi published in 1928 that introduced the classic Yagi-Uda array antenna. This antenna consists of a set of linear parallel dipoles with a spacing of about  $0.2 - 0.3\lambda$ , where the first dipole is active (i.e., fed with the signal) and the others act as passive scatterers [28]. Over the subsequent decades,

this idea has been extensively developed in various directions within the antenna theory community. One milestone is given by the introduction of reactively controlled arrays, originally proposed by Harrington in [26], where the passive scatterers can be reconfigured through the addition of programmable reactive loads to change the radiation characteristics of the antenna. Such an idea has evolved into ESPARs, which has been widely investigated to realize programmable antennas, mainly using a single RF chain and a ring of passive scatterers around it [27], [29], [30]. The typical design approach adopted for ESPARs is the characteristic mode analysis which consists of designing the loads such that the currents flowing in the elements, needed to obtain the desired radiation diagram, represent the dominant scattering mode of the structure [26]. Unfortunately, this simple approach is not accurate when applied to large structures in which secondary modes might not be negligible and hence deviate from the actual response from the desired one. Moreover, the approach cannot be applied in the case of multiple inputs, i.e., for multifunctional designs.

In more recent times, the introduction of new technologies and materials has enabled the development of new antenna structures designed to meet the demands of higher performance, flexibility, frequency, and lower cost, as required by new-generation wireless systems. Among these advancements, metasurface antennas have received particular attention. They are composed of subwavelength elements printed on a grounded dielectric slab. These antennas exploit the interaction between a cylindrical surface wave, excited by a monopole, and an anisotropic impedance boundary condition realized with passive printed elements to produce an almost arbitrary aperture field [31]. The dynamic counterpart to static metasurface antennas is the dynamic metasurface antenna (DMA), a type of traveling wave antenna with reconfigurable subwavelength apertures. Since only one RF chain is needed for each row of the planar array, DMAs offer a compelling solution, balancing flexibility with a reduction in RF chains [13], [32]. Static and dynamic metasurface antennas represent a promising avenue for the research aimed at reducing power consumption in wireless systems, thanks to their ability to shape signals at the EM level. Other recent technologies include fluid and reconfigurable antennas [33]–[35].

An important step toward holographic MIMO is the introduction of SIMs or stacked RIS [22], [36]–[38]. The concept of SIM originates from recent advances in optics and microwave circuits designed to perform machine learning tasks using layered EM surfaces to mimic a deep neural network for image processing [39], [40]. Similarly, a SIM consists of a closed vacuum container with several stacked metasurface layers. The first layer is an active planar antenna array fed by a set of RF chains. The EM wave generated by the array travels through subsequent layers composed of numerous reconfigurable meta-atoms. The last layer is in charge of radiating the EM field outward. By properly configuring the transmission properties of each meta-atom in the SIM, the system can manipulate the traveling EM wave to produce a customized waveform shape. Examples of optimization techniques for SIMs to achieve various EM wave processing functionalities can be found in [22], [36]–[38]. Specifically, [22] investigates a holographic MIMO

link where both the transmitter and the receiver use a SIM. The authors show that with a 7-layer SIM with  $\lambda/2$  meta-atom spacing, a good fit with the ideal singular value decomposition (SVD) precoding and combining tasks is obtained. In [36] and [37], optimization schemes to realize custom radiation patterns and multi-user downlink beamforming are proposed, whereas the authors in [38] demonstrate the capability to perform a 2D-Fourier transform in the wave domain. Although an energy consumption model has not yet been studied, it is expected that SIMs will be more energy efficient compared to conventional digital transceivers.

The study of SIM is still in its infancy, and the main technological and modeling challenges have yet to be fully identified. For instance, the distance between the layers must be several wavelengths to validate the currently adopted cascade model. Power losses, frequency-selective effects, and signal distortion caused by the multiple layers and the bounding box require further investigation. A key limitation of SIM is that only the final layer radiates, constraining the EM wave characteristics to those achievable with a classical planar surface or array, while the role of the hidden layers is to perform an EM transformation. Therefore, SIMs do not fully exploit the possibilities offered by EM phenomena in antenna structures for processing and radiation, thereby inheriting some limitations of standard antenna arrays, as will be detailed later.

### B. Our Contribution

In this paper, we investigate a 3D EM antenna structure, termed DSA, that offers significant flexibility by providing enhanced multifunctional processing capabilities directly at the EM level. Specifically, a DSA consists of a limited number of active antenna elements, each associated with an RF chain, surrounded by a cloud of reconfigurable passive scatterers that interact with each other in the reactive near field. As anticipated, the DSA generalizes concepts from reactively controlled arrays, their evolution into ESPARs, and SIMs. Unlike SIM, the DSA permits arbitrary distributions and couplings of passive scatterers, enabling simultaneous EM processing and radiation. Furthermore, the same configuration of scatterers can perform different EM processing functions, each associated with a distinct input to the DSA [24]. It is worth noticing that ESPARs have been mainly investigated considering only one input, narrowband signals, and limited structures [27], [29], [30].

We first characterize the input-output characteristic of the DSA as a function of its configuration parameters and provide a fully analytical model using the impedance matrix of the structure. With respect to [24], we introduce a general, physically consistent framework for modeling a wideband DSA, thereby enabling space-frequency processing capabilities. Notably, prior works on ESPARs and SIMs have been limited to narrowband signals. In contrast to previous works, we relax the assumption of ideal reactive loads by introducing reconfigurable loads modeled using realistic varactor diodes, thereby capturing the effects of reduced antenna efficiency due to dissipated power and evaluating the corresponding  $Q$ -factor. We investigate the use of an ideal power matching

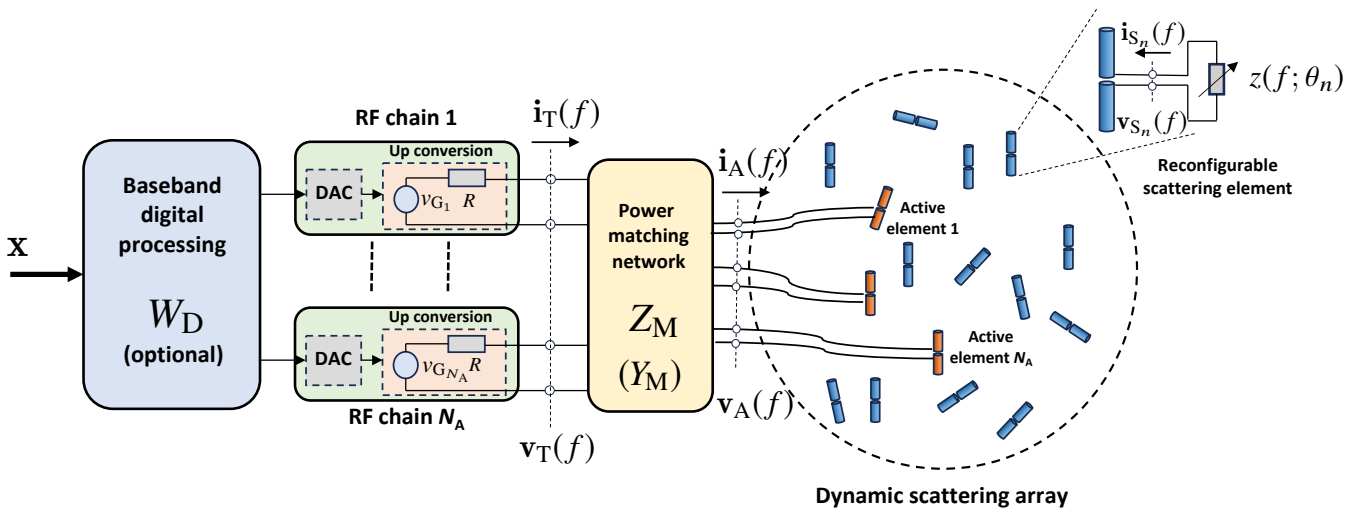


Fig. 1. Principle scheme of a dynamic scattering array with  $N_A$  active antennas connected to a matching network,  $N_A$  RF chains, and an optional baseband digital processor.

network and propose a simplified, more practical alternative, demonstrating that the latter incurs no significant performance loss. This result effectively removes the need for a complex reconfigurable power matching network. It is worth noting that the models typically used to represent ESPAR and SIM do not consider the issue of the power matching network. Building on the analytical expression of the frequency-dependent characteristics of the DSA as a function of its configuration parameters, we formulate an optimization problem to design these parameters according to the desired multifunctional and multifrequency response. The optimization also considers an optional digital precoder, which might help the optimization of the DSA. The optimization strategy is then applied to 3 different use cases of interest: superdirective beamforming, multi-user multiple-input single-output (MISO), and MIMO EM precoding. Numerical results for each use case demonstrate the great flexibility of the DSA in performing various signal processing tasks. For instance, we will show that the tight coupling of DSA elements allows for the realization of superdirectivity behavior independently of the beam's direction, in contrast to standard arrays where superdirectivity can only be achieved in the end-fire direction [41], [42].

We show that the state-of-the-art EM processing structure, i.e., the SIM, can be modeled as a particular case of a DSA, characterized by a specific block lower bidiagonal impedance matrix structure. Compared with SIM, in a DSA, all the elements contribute jointly to the processing and radiation processes, thereby enhancing flexibility with more compact structures. Indeed, in a SIM, only the elements of the last layer radiate, and thus, the maximum achievable gain is proportional to their number, similar to a conventional antenna array. Furthermore, SIMs assume only forward propagation from one layer to the next, with no coupling between the elements of each layer. While this simplifies modeling and optimization significantly, it presents critical challenges in decoupling implementation and imposes size constraints. For example, in [22] and [36], a separation of  $5\lambda$  between each layer is consid-

ered, limiting the possibility of obtaining compact structures. In contrast, our numerical results demonstrate that with a DSA, better performance can be achieved with a spacing between elements of  $\lambda/4$ , then with a significantly reduced size, thanks to the joint processing and radiation involving all the elements composing the DSA. Specifically, numerical studies confirm that, for a given geometry, the DSA outperforms a SIM in approximating the desired EM processing response while enabling the exploitation of superdirective capabilities.

### C. Notation and Definitions

Boldface capital letters are matrices (e.g.,  $\mathbf{A}$ ), where  $\mathbf{I}_N$  is the identity matrix of size  $N$ ,  $\mathbf{0}_N$  is the zero matrix of size  $N$ . With reference to a generic matrix  $\mathbf{A}$ ,  $a_{n,m} = [\mathbf{A}]_{n,m}$  represents its  $(n,m)$ th element, whereas  $\mathbf{A}^T$  and  $\mathbf{A}^H$  indicate the transpose and the conjugate transpose of  $\mathbf{A}$ , respectively. We denote with  $\mathbf{A}^\dagger$  the Moore-Penrose inverse (pseudo-inverse) and with  $\|\mathbf{A}\|_F$  the Frobenius norm of matrix  $\mathbf{A}$ . We indicate with  $\Re\{z\}$ ,  $\Im\{z\}$ , and  $z^*$ , respectively, the real part, imaginary part, and complex conjugate of the complex number  $z$ , and  $j$  the imaginary unit. The statistical expectation of a random variable  $x$  is indicated as  $\mathbb{E}\{x\}$ . Denote with  $\eta = 377 \text{ Ohm}$  the free-space impedance and  $c$  the speed of light.

### D. Paper Organization

The rest of the paper is organized as follows: Sec. II introduces the general framework to model the DSA. The optimization of the parameters characterizing the DSA is addressed in general in Sec. III, and further declined in 3 use cases. Numerical results associated with the 3 use cases are provided in Sec. IV. Finally, the conclusions are drawn in Sec. V.

## II. DYNAMIC SCATTERING ARRAY (DSA) MODELING

With reference to Fig. 1, a DSA is composed of  $N_A$  active antennas, each of them connected to an RF

chain, surrounded by a cloud of  $N_S$  reconfigurable passive scatterers interacting in the reactive near field for a total of  $N = N_A + N_S$  elements. In the figure, elements are seemingly deployed at random to emphasize that the proposed framework is applicable to arbitrary 2D and 3D geometries. The frequency-dependent response of the DSA can be changed by loading each antenna element using a reconfigurable load of frequency-dependent impedance  $z(f; \theta)$ , which is a function of parameter  $\theta$  that affects the impedance according to the specific load implementation technology, as it will be detailed in Sec. IV-A. Denote with  $\boldsymbol{\theta} = [\theta_1, \theta_2, \dots, \theta_{N_S}]$  the set of reconfigurable parameters of the  $N_S$  loads and with  $\mathbf{Z}_S(f; \theta) = \text{diag}(z(f; \theta_1), z(f; \theta_2), \dots, z(f; \theta_{N_S}))$  the diagonal matrix collecting the corresponding set of loads' impedances.

The DSA can be modeled as a linear frequency-selective  $N$ -port network. In a compact description, we define  $\mathbf{v}_A(f) \in \mathbb{C}^{N_A \times 1}$  and  $\mathbf{i}_A(f) \in \mathbb{C}^{N_A \times 1}$  the complex voltage and current envelopes (in the following denoted simply as voltages and currents) at the ports of the  $N_A$  active antennas at the generic symbol time,<sup>1</sup> and  $\mathbf{v}_S(f) \in \mathbb{C}^{N_S \times 1}$  and  $\mathbf{i}_S(f) \in \mathbb{C}^{N_S \times 1}$  the voltages and currents at the ports of the  $N_S$  scatterers. Since voltages and currents carry information, they must be treated as random variables for a given frequency. We collect all the currents and voltages at the  $N$  ports of the DSA in the vectors

$$\mathbf{i}(f) = \begin{bmatrix} \mathbf{i}_A(f) \\ \mathbf{i}_S(f) \end{bmatrix} \in \mathbb{C}^{N \times 1} \quad \mathbf{v}(f) = \begin{bmatrix} \mathbf{v}_A(f) \\ \mathbf{v}_S(f) \end{bmatrix} \in \mathbb{C}^{N \times 1}. \quad (1)$$

All the interactions between the elements of the DSA are captured by the impedance matrix  $\mathbf{Z}(f) \in \mathbb{C}^{N \times N}$ , which does not depend on the reconfigurable loads, and relates the voltages and currents of the  $N$  ports as  $\mathbf{v}(f) = \mathbf{Z}(f) \mathbf{i}(f)$ . It can be computed once during the design of the DSA according to the technology adopted. In Sec. IV, an example will be given. In particular, the  $(m, n)$ th element of  $\mathbf{Z}(f)$  represents the mutual coupling coefficient between the  $n$ th and  $m$ th elements obtained as the ratio between the open-circuit voltage observed at the  $m$ th port and the excitation sinusoidal current at frequency  $f$  applied to the  $n$ th port supposing that the remaining ports are kept open (no current flow) [43]. It is convenient to divide the impedance matrix  $\mathbf{Z}(f)$  into the submatrices  $\mathbf{Z}_{AA}(f)$ ,  $\mathbf{Z}_{AS}(f)$ ,  $\mathbf{Z}_{SA}(f)$ , and  $\mathbf{Z}_{SS}(f)$  so that we can write

$$\begin{bmatrix} \mathbf{v}_A(f) \\ \mathbf{v}_S(f) \end{bmatrix} = \begin{bmatrix} \mathbf{Z}_{AA}(f) & \mathbf{Z}_{AS}(f) \\ \mathbf{Z}_{SA}(f) & \mathbf{Z}_{SS}(f) \end{bmatrix} \cdot \begin{bmatrix} \mathbf{i}_A(f) \\ \mathbf{i}_S(f) \end{bmatrix}. \quad (2)$$

The voltages  $\mathbf{v}_A(f)$  and currents  $\mathbf{i}_A(f)$  at the input ports of the DSA are related by the input impedance of the DSA  $\mathbf{Z}_A(f; \theta) \in \mathbb{C}^{N_A \times N_A}$  as  $\mathbf{v}_A(f) = \mathbf{Z}_A(f; \theta) \mathbf{i}_A(f)$ . By elaborating (2) and considering that at the scatterers' ports it is  $\mathbf{v}_S(f) = -\mathbf{Z}_S(f; \theta) \mathbf{i}_S(f)$ , we obtain

$$\mathbf{Z}_A(f; \theta) = \mathbf{Z}_{AA}(f) - \mathbf{Z}_{AS}(f) (\mathbf{Z}_{SS}(f) + \mathbf{Z}_S(f; \theta))^{-1} \mathbf{Z}_{SA}(f) \quad (3)$$

which depends on parameters  $\theta$  through the scatterers' loads  $\mathbf{Z}_S(f; \theta)$ . For further convenience, possible dissipative components in the antenna elements are accounted for as additional

<sup>1</sup>For notation convenience, we omit the time dependence.

resistive terms in the loads  $\mathbf{Z}_S(f; \theta)$ . As a consequence, the radiated power  $P_{\text{rad}}(f)$  at frequency  $f$  can be evaluated as

$$P_{\text{rad}}(f) = \mathbb{E} \left\{ \mathbf{i}(f)^H \Re \{ \mathbf{Z}(f) \} \mathbf{i}(f) \right\} \quad (4)$$

whereas the reactive power is

$$P_{\text{react}}(f) = \mathbb{E} \left\{ \mathbf{i}(f)^H \Im \{ \mathbf{Z}(f) \} \mathbf{i}(f) \right\} \quad (5)$$

from which the  $Q$ -factor of the structure can be obtained as  $Q(f) = P_{\text{react}}(f)/P_{\text{rad}}(f)$ . The inverse of the  $Q$ -factor can be used as a rough estimate of the bandwidth of the DSA when  $Q \gg 1$  [43].

The  $N_A$  active elements are connected to the  $N_A$  RF chains, including digital-to-analog converter (DAC) and up-conversion stages, through a  $2N_A$ -port power matching network whose purpose is to maximize the power transfer between the RF chains and the DSA. The available transmitted power at the output of the RF chains is

$$P_T(f) = \frac{\mathbb{E} \{ \mathbf{v}_G(f)^H \mathbf{v}_G(f) \}}{4R} \quad (6)$$

with  $\mathbf{v}_G(f) = [v_{G1}(f), v_{G2}(f), \dots, v_{GN_A}(f)]^T$  representing the open-circuit voltages of the RF chains and  $R$  being the internal resistance of each chain. It coincides with the power transferred to the DSA only when a perfect power-matching network is introduced.

In the following, we consider two different implementations of the network connecting the DSA and the  $N_A$  RF chains: a) Perfect matching network; b) Simplified (not perfect) matching network.

#### A. Perfect Matching Network

In this implementation, the relationship between the voltages and the currents present at the ports of the matching network is given by

$$\begin{bmatrix} \mathbf{v}_T(f) \\ \mathbf{v}_A(f) \end{bmatrix} = \mathbf{Z}_M(f; \theta) \begin{bmatrix} \mathbf{i}_T(f) \\ -\mathbf{i}_A(f) \end{bmatrix} \quad (7)$$

where, assuming no losses in the power matching network,  $\mathbf{Z}_M(f; \theta)$  is equal to [41]

$$\mathbf{Z}_M(f; \theta) = \begin{bmatrix} \mathbf{0}_{N_A} & -J\sqrt{R} \Re \{ \mathbf{Z}_A(f; \theta) \}^{\frac{1}{2}} \\ -J\sqrt{R} \Re \{ \mathbf{Z}_A(f; \theta) \}^{\frac{1}{2}} & -J\Im \{ \mathbf{Z}_A(f; \theta) \} \end{bmatrix} \quad (8)$$

As it can be noticed from (8), the matching network depends on the DSA input impedance  $\mathbf{Z}_A(f; \theta)$  and hence on the parameters  $\theta$ . Therefore, for a given configuration of the DSA, the matching network should be changed accordingly. This is possible using, for instance, adaptive matching networks [44]. In case a fixed network is employed instead, then not all the available power would be transferred to the DSA with a consequent reduction of efficiency. An alternative and more practical solution is proposed in Sec. II-B. With the perfect matching network, it turns out that  $\mathbf{v}_T(f) = R \mathbf{i}_T(f)$  and the actual power transferred to the DSA coincides with the available power

$$P_a(f) = \frac{\mathbb{E} \{ \mathbf{v}_T(f)^H \mathbf{v}_T(f) \}}{R} = P_T(f). \quad (9)$$

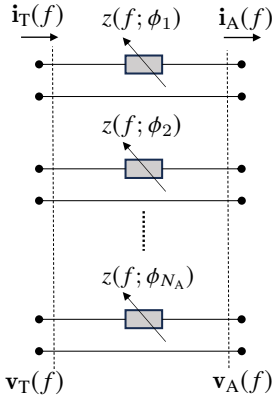


Fig. 2. Simplified matching network.

From (7) and (8) it is

$$\mathbf{i}_A(f) = \frac{1}{j2\sqrt{R}} \Re \{\mathbf{Z}_A(f; \theta)\}^{-\frac{1}{2}} \mathbf{v}_G(f). \quad (10)$$

Moreover, we have

$$\mathbf{i}(f) = \begin{bmatrix} \mathbf{I}_{N_A} \\ -(\mathbf{Z}_{SS}(f) + \mathbf{Z}_S(f; \theta))^{-1} \mathbf{Z}_{SA}(f) \end{bmatrix} \cdot \mathbf{i}_A(f). \quad (11)$$

By combining (10) and (11), we obtain a compact relationship between the open-circuit voltages of the RF chains  $\mathbf{v}_G(f)$  and the total current  $\mathbf{i}(f)$  flowing in the DSA

$$\mathbf{i}(f) = \mathbf{W}_{EM}(f; \psi) \mathbf{v}_G(f) \quad (12)$$

where

$$\mathbf{W}_{EM}(f; \psi) = \frac{1}{j2\sqrt{R}} \begin{bmatrix} \Re \{\mathbf{Z}_A(f; \theta)\}^{-\frac{1}{2}} \\ -(\mathbf{Z}_{SS}(f) + \mathbf{Z}_S(f; \theta))^{-1} \mathbf{Z}_{SA}(f) \Re \{\mathbf{Z}_A(f; \theta)\}^{-\frac{1}{2}} \end{bmatrix} \quad (13)$$

accounts for the EM-level signal processing operated by the reconfigurable DSA as a function of the parameters  $\psi = \{\theta\}$ .

The radiated power is  $P_{rad}(f) = \eta_d(f) P_T(f)$ , where  $\eta_d(f) = P_{rad}(f)/P_a(f) = 1 - P_d(f)/P_a(f)$  represents the power loss due to dissipation at frequency  $f$  and  $P_d(f) = \mathbb{E}\{\mathbf{i}_S(f)^H \Re \{\mathbf{Z}_S(f; \theta)\} \mathbf{i}_S(f)\}$  is the dissipated power.

### B. Simplified Matching Network

We propose the simplified matching network represented in the scheme shown in Fig. 2, where  $N_A$  additional reconfigurable impedances  $\mathbf{Z}_L(f; \phi) = [z(f; \phi_1), z(f; \phi_2), \dots, z(f; \phi_{N_A})]^\top$  are added at the input of the active elements of the DSA so that the matching task enters the optimization process. The vector  $\phi = [\phi_1, \phi_2, \dots, \phi_{N_A}]$  collects the corresponding parameters to be optimized. The relationship between the voltages and the currents present at the ports of the matching network can be expressed through the admittance matrix<sup>2</sup> given by

$$\begin{bmatrix} \mathbf{i}_T(f) \\ -\mathbf{i}_A(f) \end{bmatrix} = \mathbf{Y}_M(f; \phi) \begin{bmatrix} \mathbf{v}_T(f) \\ \mathbf{v}_A(f) \end{bmatrix} \quad (14)$$

where

$$\mathbf{Y}_M(f; \phi) = \mathbf{Z}_L(f; \phi)^{-1} \begin{bmatrix} \mathbf{I}_{N_A} & -\mathbf{I}_{N_A} \\ -\mathbf{I}_{N_A} & \mathbf{I}_{N_A} \end{bmatrix}. \quad (15)$$

Using (14) and (15), the open-circuit voltage of the RF chains is  $\mathbf{v}_G(f) = \mathbf{Q}(f, \phi) \mathbf{i}_A$ , where  $\mathbf{Q}(f, \phi) = \mathbf{Z}_A(f; \theta) + \mathbf{Z}_L(f; \phi) + R \mathbf{I}_{N_A}$ . The relationship between  $\mathbf{v}_G(f)$  and  $\mathbf{i}(f)$  is still given by (12), where now

$$\mathbf{W}_{EM}(f; \psi) = \begin{bmatrix} \mathbf{Q}(f, \phi)^{-1} \\ -(\mathbf{Z}_{SS}(f) + \mathbf{Z}_S(f; \theta))^{-1} \mathbf{Z}_{SA}(f) \mathbf{Q}(f, \phi)^{-1} \end{bmatrix} \quad (16)$$

accounts for the EM-level signal processing operated by the reconfigurable DSA as a function of the overall set of parameters  $\psi = \{\theta; \phi\}$ .

In this case, the actual power transferred to the DSA is  $P_a(f) = \eta_m(f) P_T(f)$ , where  $\eta_m(f) = 1$  with the perfect matching network, and the radiated power is  $P_{rad}(f) = \eta_d(f) \eta_m(f) P_T(f)$ , where  $\eta_d(f) = 1 - P_d(f)/P_a(f)$ , with  $P_d(f) = \mathbb{E}\{\mathbf{i}_S(f)^H \Re \{\mathbf{Z}_S(f; \theta)\} \mathbf{i}_S(f)\} + \mathbb{E}\{\mathbf{i}_A(f)^H \Re \{\mathbf{Z}_L(f; \phi)\} \mathbf{i}_A(f)\}$  accounting for the power dissipated in the DSA and the matching network.

### C. Digital Processing

We also foresee an optional baseband linear processing block implemented in the digital domain (digital precoder), described by the matrix  $\mathbf{W}_D \in \mathbb{C}^{N_A \times N_A}$ , whose input is represented by the information vector  $\mathbf{x}(f) \in \mathbb{C}^{N_A \times 1}$  to be transmitted. The matrix  $\mathbf{W}_D$  relates the transmitted information vector  $\mathbf{x}(f)$  and the open-circuit voltages  $\mathbf{v}_G(f)$  of the RF chains, i.e.,  $\mathbf{v}_G(f) = \mathbf{W}_D \mathbf{x}(f)$ . In the following, we impose the arbitrary normalization  $\|\mathbf{W}_D\|_F = \sqrt{4RN_A}$ . Such a normalization ensures that  $\mathbb{E}\{\mathbf{x}(f)^H \mathbf{x}(f)\} = P_T(f)$ , where  $P_T(f)$  is the (available) transmitted power, as typically assumed in the signal processing community.

The reconfigurable parameters  $\psi$  along with the elements of matrix  $\mathbf{W}_D$  represent the set of parameters to be optimized to obtain the desired processing functionality, as will be described later.

### D. Particular Case: SIM Modeling

In this section, we show how the general framework illustrated in the previous section can be made particular to model a SIM.

Suppose the  $N_S$  reconfigurable scattering elements are organized in layers, where the  $l$ th layer is composed of  $N_l$  elements, such that  $\sum_{l=1}^L N_l = N_S$ . A typical assumption for modeling a SIM is to consider no coupling between elements belonging to the same layer, and only forward propagation, meaning that coupling takes place only between each element of layer  $l$  and the elements of layer  $l+1$ , but not vice versa. This

<sup>2</sup>In this case, the corresponding impedance matrix cannot be defined.

translates into the following block lower bidiagonal structure of the impedance matrix of the DSA

$$\mathbf{Z}(f) = \begin{bmatrix} \mathbf{Z}_{AA}(f) & 0 & 0 & \dots & 0 \\ \mathbf{B}_1(f) & \mathbf{A}_1(f) & 0 & \dots & 0 \\ 0 & \mathbf{B}_2(f) & \mathbf{A}_2(f) & \dots & 0 \\ \vdots & \vdots & \vdots & \ddots & \vdots \\ 0 & 0 & 0 & \dots & \mathbf{A}_L(f) \end{bmatrix} \quad (17)$$

where  $\mathbf{A}_l(f) \in \mathbb{C}^{N_l \times N_l}$ ,  $l = 1, 2, \dots, L$ , is a diagonal matrix representing the self-impedance of the scattering elements belonging to layer  $l$ . Also  $\mathbf{Z}_{AA}(f) \in \mathbb{C}^{N_A \times N_A}$  is, in this case, a diagonal matrix associated to the self-impedance of the  $N_A$  active antennas. Matrix  $\mathbf{B}_l(f) \in \mathbb{C}^{N_l \times N_{l-1}}$ , for  $l = 1, 2, \dots, L$ , accounts for the (forward) coupling between layer  $l$  and layer  $l - 1$  (when  $l = 1$ , the coupling is with the active antennas, and  $N_{l-1} = N_A$ ). From simple matrix manipulations, since  $\mathbf{Z}_{AS}(f) = \mathbf{0}$ , the DSA input matrix is simply given by  $\mathbf{Z}_A(f; \theta) = \mathbf{Z}_{AA}(f)$ , which does not depend on the DSA configuration  $\theta$ . Therefore, there is no need for an adaptive power matching network (we set  $\mathbf{Z}_L(f; \phi) = 0$ ). For instance, the  $N_A$  active elements can be matched to the RF chain internal impedance  $R$ , thus leading to  $\mathbf{Z}_A(f; \theta) = R \mathbf{I}_{N_A}$  and  $\mathbf{Q}(f, \phi) = \mathbf{Q} = 2R \mathbf{I}_{N_A}$ . Denote with  $\mathbf{i}_l(f) \in \mathbb{C}^{N_l \times 1}$ , for  $l = 1, 2, \dots, L$ , the currents flowing in the elements of the  $l$ th layer. It follows that

$$\begin{bmatrix} \mathbf{i}_A(f) \\ \mathbf{i}_1(f) \\ \mathbf{i}_2(f) \\ \vdots \\ \mathbf{i}_L(f) \end{bmatrix} = \begin{bmatrix} \mathbf{Q}^{-1} \\ -(\mathbf{Z}_{SS}(f) + \mathbf{Z}_S(f; \theta))^{-1} \mathbf{Z}_{SA}(f) \mathbf{Q}^{-1} \end{bmatrix} \mathbf{v}_G(f). \quad (18)$$

In a typical SIM, only the last layer is designed to radiate outside the structure; therefore in this case, the matrix  $\mathbf{W}_{EM}(f; \psi) \in \mathbb{C}^{N_L \times N_A}$  is the submatrix in (18) which puts in relationship the input voltages  $\mathbf{v}_G(f)$  with only the currents  $\mathbf{i}_L(f)$  of the last layer. By exploiting the particular block lower bidiagonal structure of  $\mathbf{Z}_{SS}(f) + \mathbf{Z}_S(f; \theta)$ , and by applying the iterative Schur complement, we obtain

$$\mathbf{W}_{EM}(f; \psi) = (-1)^L \mathbf{B}_L(f) \Phi_L(f; \theta) \dots \dots \Phi_2(f; \theta) \mathbf{B}_2(f) \Phi_1(f; \theta) \mathbf{B}_1(f) \mathbf{Q}^{-1} \quad (19)$$

having defined the diagonal matrix

$$\Phi_l(f; \theta) = (\mathbf{A}_l(f) + \text{diag}(z(f; \theta_{p_l+1}), \dots, z(f; \theta_{p_{l+1}})))^{-1} \quad (20)$$

for  $l = 1, 2, \dots, L$ , with  $p_l = \sum_{i=1}^{l-1} N_i$ . Equation (19) reveals that the typical modelling of a SIM can be obtained as a particular case of our general framework. The characteristic chain structure of (19) enables the adoption of gradient descent algorithms based on error backpropagation, similar to those used in deep neural networks [38]. Nevertheless, while the characteristics of the SIM allow for simplified optimization schemes, as already pointed out, only the last layer contributes to the radiation, thus limiting the flexibility of the SIM

compared to a DSA. It is worth underlining that model (19) is based on relatively oversimplified assumptions that do not take into account nonidealities such as couplings between elements of the same layer or backscattering from subsequent layers. Such non-idealities can be easily included in our general framework through the impedance matrix (17), which, however, would lose its block lower bidiagonal structure, and a more general optimization scheme would be required, as proposed in the next section.

### III. DSA OPTIMIZATION

Consider now  $T$  test points located in positions  $\mathbf{t}_t$ , with  $t = 1, 2, \dots, T$ , and that in each test point, a conventional receiving wideband antenna is used to receive the signal with gain  $G_R$ . As commonly done in the literature, we assume that the test points are located in the radiative region of the DSA and the receiving antennas do not affect the DSA. As examples, the set of  $T$  antennas could represent a conventional receiving antenna array of a MIMO system or users located in different positions. In addition, we suppose a multicarrier signaling with total bandwidth  $W$  using  $K$  subcarriers at frequencies  $f_k = f_0 + (k-1)W/K$ , for  $k = 1, 2, \dots, K$ . To be general, we consider that a different digital processing matrix  $\mathbf{W}_{D_k}$ , for  $k = 1, 2, \dots, K$ , is applied to each subcarrier.

The useful component (i.e., without noise) of the received signal at the test positions at frequency  $f_k$  is

$$\begin{aligned} \mathbf{y}(f_k) &= \mathbf{H}_c(f_k) \mathbf{i}(f_k) + \mathbf{n}(f_k) \\ &= \mathbf{H}_c(f_k) \mathbf{W}_{EM}(f_k; \psi) \mathbf{W}_{D_k} \mathbf{x}(f_k) + \mathbf{n}(f_k) \\ &= \mathbf{H}_k(\psi, \mathbf{W}_{D_k}) \mathbf{x}(f_k) + \mathbf{n}(f_k) \end{aligned} \quad (21)$$

where  $\mathbf{n}(k)$  is the zero-mean complex Gaussian additive white Gaussian noise (AWGN) with covariance matrix  $\sigma^2 \mathbf{I}_K$ ,  $\mathbf{H}_c(f_k) \in \mathbb{C}^{T \times N}$  is the transimpedance matrix of the radio channel accounting for the propagation effects, and  $\mathbf{H}_k(\psi, \mathbf{W}_{D_k}) \in \mathbb{C}^{T \times N_A}$  represents the end-to-end baseband equivalent channel matrix as commonly defined in signal processing.

In this section, we illustrate a possible optimization strategy of the DSA along with its application to 3 different use cases. Numerical results associated with each use case will be reported in Sec. IV.

#### A. Joint Optimization of the DSA and the Digital Precoder

For a given propagation scenario characterized by the transimpedance matrix  $\mathbf{H}_c(f)$ ,  $T$  test points, and  $K$  frequencies  $\{f_k\}$ , suppose we fix a specification  $\mathbf{H}_k^{(opt)} \in \mathbb{C}^{T \times N_A}$  on the desired end-to-end channel matrix (i.e., our desired processing). The reconfigurable parameters of the DSA and the digital precoder can be obtained by solving the following constrained optimization problem:

$$\begin{aligned} &\underset{\psi, \alpha, \{\mathbf{W}_{D_k}\}}{\text{minimize}} \sum_{k=1}^K \left\| \alpha_k \mathbf{H}_c(f_k) \mathbf{W}_{EM}(f_k; \psi) \mathbf{W}_{D_k} - \mathbf{H}_k^{(opt)} \right\|_F^2 \\ &\text{s.t. } \|\mathbf{W}_{D_k}\|_F^2 = 4RN_A \quad k = 1, 2, \dots, K \end{aligned} \quad (22)$$

where  $\alpha = \{\alpha_1, \alpha_2, \dots, \alpha_K\}$  with the scalars  $\alpha_k \in \mathbb{R}$  accounting for the possible lack in the link budget to achieve  $\mathbf{H}_k^{(\text{opt})}$  that has to be eventually coped with increased transmitted power. It is worth noting that the  $n$ th column of  $\mathbf{H}_k^{(\text{opt})}$  represents the desired response of the DSA at the  $T$  test points to the  $n$ th input data stream  $x_n(f_k)$  at frequency  $f_k$  (alias the  $n$ th processing function). Therefore, the minimization of (22) leads to a configuration for which the DSA approximates the multi-functional processing of the inputs at the EM level.

Unfortunately, in general, the constrained optimization problem in (22) is not convex thus making its numerical solution more challenging. A possible approach to translating it into an unconstrained optimization problem is to resort to the following alternate optimization procedure:

- STEP 0: We set the candidate vector  $\hat{\psi}$  to an initial guess value, for instance randomly chosen.
- STEP 1:

For a fixed  $\hat{\psi}$ , it is possible to find in closed form the values of  $\mathbf{W}_{D_k}$  and  $\alpha_k$  that minimize the objective transfer function and satisfy the constraint in (22). In particular, we solve the following equation

$$\alpha_k \mathbf{H}_c(f_k) \mathbf{W}_{EM}(f_k; \hat{\psi}) \mathbf{W}_{D_k} = \mathbf{H}_k^{(\text{opt})} \quad (23)$$

of which the minimum norm solution is

$$\alpha_k \mathbf{W}_{D_k} = (\mathbf{H}_c(f_k) \mathbf{W}_{EM}(f_k; \hat{\psi}))^\dagger \mathbf{H}_k^{(\text{opt})}. \quad (24)$$

The corresponding values of  $\hat{\alpha}_k$  and  $\hat{\mathbf{W}}_{D_k}$  are, therefore,

$$\hat{\alpha}_k = \frac{1}{\sqrt{4RN_A}} \left\| (\mathbf{H}_c(f_k) \mathbf{W}_{EM}(f_k; \hat{\psi}))^\dagger \mathbf{H}_k^{(\text{opt})} \right\|_F \quad (25)$$

and

$$\hat{\mathbf{W}}_{D_k} = \frac{1}{\hat{\alpha}_k} (\mathbf{H}_c(f_k) \mathbf{W}_{EM}(f_k; \hat{\psi}))^\dagger \mathbf{H}_k^{(\text{opt})}. \quad (26)$$

- STEP 2:

Starting from the candidates  $\hat{\alpha}$  and  $\hat{\mathbf{W}}_{D_k}$  from STEP 1, the following unconstrained minimization problem involving only  $\psi$  is solved numerically

$$\hat{\psi} = \arg \min_{\psi} \sum_{k=1}^K \left\| \hat{\alpha}_k \mathbf{H}_c(f_k) \mathbf{W}_{EM}(f_k; \psi) \hat{\mathbf{W}}_{D_k} - \mathbf{H}_k^{(\text{opt})} \right\|_F^2. \quad (27)$$

- STEP 3: Repeat STEPS 1 and 2 for a given number  $N_{\text{alt}}$  iterations or until no significant variations of the parameters take place.

### B. Use Case 1: Superdirective Beam Forming

The inclusion of the digital precoder, while not strictly necessary, may aid in the optimization process of the DSA by handling a portion of the processing when  $N_A > 1$ . If omitted, we set  $\hat{\mathbf{W}}_{D_k} = \mathbf{W}_{D_k} = \sqrt{4R} \mathbf{I}_{N_A}$ , and only proceed with STEP 2 once. Of course, alternative optimization problems apart from (22) can also be considered, such as those involving the  $Q$ -factor as an optimization target or constraint. In many applications (e.g., beam steering, as in use case 1 below), the optimization process can be performed offline, computed

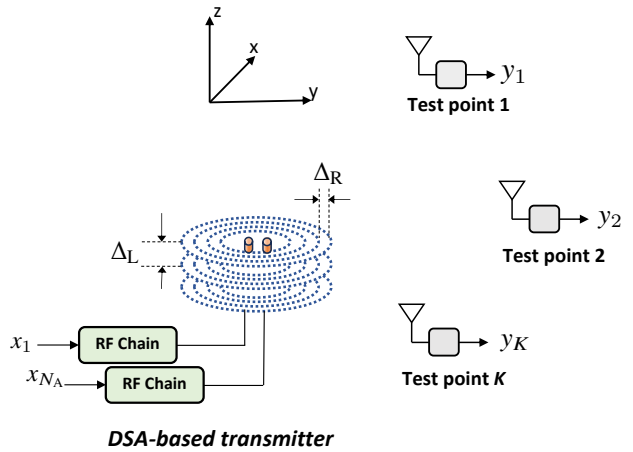


Fig. 3. Use case 1: Single RF chain DSA for superdirective beamforming.

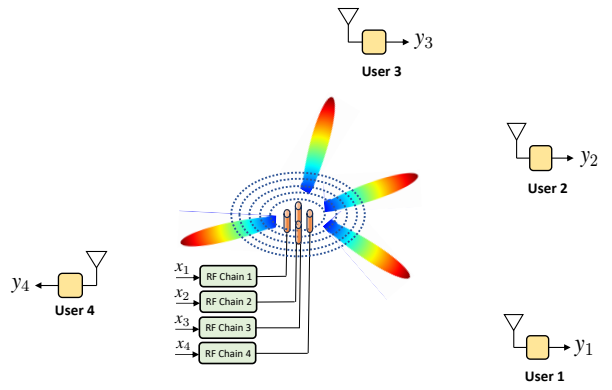


Fig. 4. Use case 2: Multi-user downlink MISO with a DSA.

once to create a dictionary of various DSA parameters for different steering directions of interest or, more broadly, different beam forms. In such cases, the complexity of the optimization algorithm is not a concern. However, in other scenarios, performing optimization offline may not be feasible, necessitating online optimization based, for example, on the channel state information (CSI) of  $\mathbf{H}_c(f_k)$ . In this situation, developing efficient algorithms to minimize (27), potentially considering the structure of  $\mathbf{W}_{EM}(f_k; \hat{\psi})$ , becomes pertinent. This aspect exceeds the scope of this paper and is reserved for future investigations. In the numerical results, the standard numerical tool based on the quasi-Newton method [45] with  $N_i$  iterations is utilized to minimize (27).

Suppose we want to design a single-input DSA ( $N_A = 1$ , no digital precoding) realizing a generic radiation diagram associated with subcarrier  $k$ , for instance, imposing that at the test locations  $\mathbf{t}_t$ , the channel matrix  $[\mathbf{H}_k^{(\text{opt})}]_{t,1}$ ,  $t = 1, 2, \dots, T$ , assumes some desired values (see Fig. 3). For instance, one might define a uniform set of test points  $\mathbf{t}_t = [d \sin \phi_t, 0, d \cos \phi_t]^T$  on the  $x-y$  plane a distance  $d$  in the far-field region of the DSA, with  $\phi_t = 2\pi t/T$ , and maximize the radiation diagram at the  $t = \tilde{t}$ th direction  $\phi_{\tilde{t}}$  (beam steering). This can be achieved by setting  $[\mathbf{H}_k^{(\text{opt})}]_{t,1} = \sqrt{P_R}$ ,

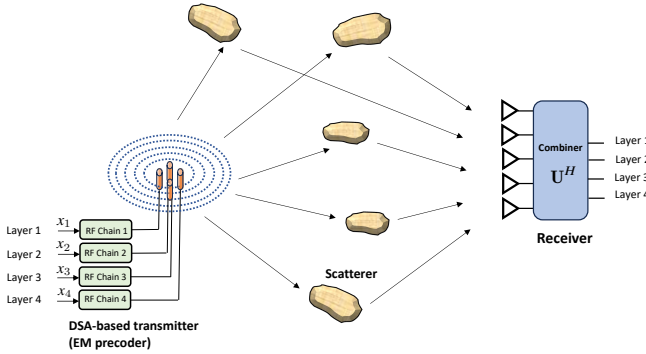


Fig. 5. Use case 3: DSA working as a MIMO EM precoder.

for  $t = \tilde{t}$ , and zero otherwise, being  $P_R$  the desired received power. As it will be shown in the numerical results, a dedicated radiation diagram can be obtained for each subcarrier. It is worth noticing that, in principle, only the optimization at the single test point  $\mathbf{t}_{\tilde{k}}$ , i.e.,  $T = 1$ , would suffice to obtain the desired beam steering result. However, the addition of many other test points set to zero helps the minimization algorithm to speed up and avoid the convergence to bad local minima.

### C. Use Case 2: Multi-user MISO

In this second use case, we consider a multi-user MISO downlink scenario shown in Fig. 4, where an DSA with  $N_A$  RF chains (one per user) has to be designed to serve simultaneously  $T = N_A$  single-antenna users located in generic positions  $\mathbf{t}_t$ ,  $t = 1, 2, \dots, T$ , by maximizing the signal-to-interference noise ratio (SINR) at each user according to the zero-forcing criterium [46]. Users can be both in the radiating near-field and far-field regions of the DSA.

Given the channel transimpedance matrix  $\mathbf{H}_c(f_k) = [\mathbf{h}_c(f_k)]_1; [\mathbf{h}_c(f_k)]_2; \dots; [\mathbf{h}_c(f_k)]_{N_A}]$ , where  $[\mathbf{h}_c(f_k)]_t$  is the  $N \times 1$  channel vector associated with the  $t$ th user, the zero-forcing precoding matrix is  $\mathbf{V}_k = \beta_k \mathbf{H}_c(f_k)^\dagger$ , where  $\beta_k$  is a normalization factor to make  $\mathbf{V}_k$  unitary, i.e.,  $\mathbf{V}_k^\dagger \mathbf{V}_k = \mathbf{I}_N$  [46]. Therefore, the DSA and the digital precoder must be designed such that

$$\mathbf{W}_{EM}(f_k; \psi) \mathbf{W}_{D_k} = \mathbf{V}_k = \beta_k \mathbf{H}_c(f_k)^\dagger \quad (28)$$

leading to

$$\begin{aligned} \mathbf{y}(f_k) &= \mathbf{H}_c(f_k) \mathbf{W}_{EM}(f_k; \psi) \mathbf{W}_{D_k} \mathbf{x}(f_k) + \mathbf{n}(f_k) \\ &= \mathbf{H}_c(f_k) \mathbf{H}_c(f_k)^\dagger \mathbf{x}(f_k) + \mathbf{n}(f_k). \end{aligned} \quad (29)$$

This is equivalent to setting  $\mathbf{H}_k^{(opt)} = \mathbf{H}_c(f_k) \mathbf{H}_c(f_k)^\dagger$  in the optimization problem in (22).

### D. Use Case 3: MIMO EM Precoder

In this use case, we consider a MIMO communication link with a receiving conventional uniform linear array (ULA) with  $T$  elements spaced at  $\lambda/2$  illustrated in Fig. 5. The purpose is to design the DSA in such a way an optimal multi-layer MIMO link is established between the transmitter and the receiver. It is well known from MIMO theory that for a given generic propagation scenario with channel transimpedance matrix  $\mathbf{H}_c(f_k)$

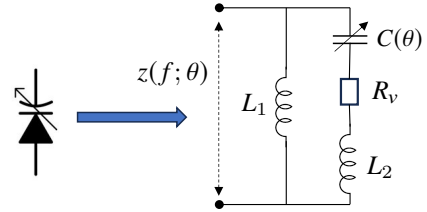


Fig. 6. Equivalent circuit model of a varactor diode used as reconfigurable load.

characterized by rank  $r$ , up to  $r$  parallel orthogonal links (layers) can be established between the transmitter and the receiver on which  $r$  independent data stream can be transmitted [46]. To exploit all of them, it must be  $N_A = r$  and the DSA must implement a suitable precoding strategy, i.e., act as an *EM precoder*.

Let us introduce the SVD of the channel transimpedance

$$\mathbf{H}_c(f_k) = \mathbf{U}_k \Lambda_k \mathbf{V}_k^\dagger \quad (30)$$

where  $\mathbf{U}_k$  and  $\mathbf{V}_k$  contain the left and right eigenvectors, respectively, and  $\Lambda_k$  is a diagonal matrix gathering the singular values of the channel transimpedance matrix  $\mathbf{H}_c(f_k)$ . A typical MIMO setup, assuming the CSI is available at the transmitter, requires a precoding operation  $\mathbf{V}_k$  at the transmitter and a combining operation  $\mathbf{U}_k^\dagger$  at the receiver such that the channel is diagonalized, i.e., the end-to-end channel matrix is proportional to the diagonal matrix  $\Lambda_k$ . Assuming the receiver performs the combining operation  $\tilde{\mathbf{y}}(f_k) = \mathbf{U}_k^\dagger \mathbf{y}(f_k)$ , the MIMO channel is diagonalized if we design the DSA implementing the precoding  $\mathbf{V}_k$  by setting

$$\mathbf{W}_{EM}(f_k; \psi) \mathbf{W}_{D_k} = \mathbf{V}_k \quad (31)$$

or, equivalently,

$$\mathbf{H}_k^{(opt)} = \mathbf{U}_k \Lambda_k. \quad (32)$$

In this manner, it results

$$\begin{aligned} \tilde{\mathbf{y}}(f_k) &= \mathbf{U}_k^\dagger \mathbf{H}_c(f_k) \mathbf{W}_{EM}(f_k; \psi) \mathbf{W}_{D_k} \mathbf{x}(f_k) + \mathbf{n}(f_k) \\ &= \mathbf{U}_k^\dagger \mathbf{H}_c(f_k) \mathbf{W}_{EM}(f_k; \psi) \mathbf{W}_{D_k} \mathbf{x}(f_k) + \mathbf{n}(f_k) \\ &= \Lambda_k \mathbf{V}_k^\dagger \mathbf{V}_k \mathbf{x}(f_k) + \mathbf{n}(f_k) = \Lambda_k \mathbf{x}(f_k) + \mathbf{n}(f_k) \end{aligned} \quad (33)$$

and  $N_A$  parallel communication layers can be established. The designed DSA implements the optimal precoding at the EM level, thus saving  $2N^2$  multiplications and sums in the digital domain, by using no more than  $N_A = r$  RF chains (i.e., the minimum possible value), which is much simpler and less energy consuming than any conventional full digital or hybrid solution.

In our numerical investigations, we discovered that a more robust optimization is obtained by solving the following equivalent problem instead of (27)

$$\underset{\psi, \alpha, \{\mathbf{W}_{D_k}\}}{\text{minimize}} \sum_{k=1}^K \left\| \hat{\alpha}_k \mathbf{U}_k^\dagger \mathbf{H}_c(f_k) \mathbf{W}_{EM}(f_k; \psi) \mathbf{W}_{D_k} - \Lambda_k \right\|_{\text{F}}^2 \quad (34)$$

that consists in multiplying both terms in (27) by  $\mathbf{U}^\dagger(f_k)$ .

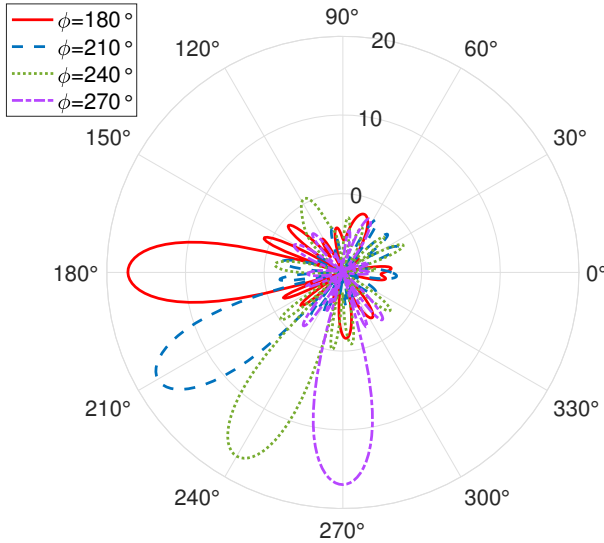


Fig. 7. Radiation diagram of a disk-shaped DSA ( $L_R = 1$ ) with  $N_A = 1$ ,  $\Delta_R = \lambda/4$ , and  $L = 5$ .

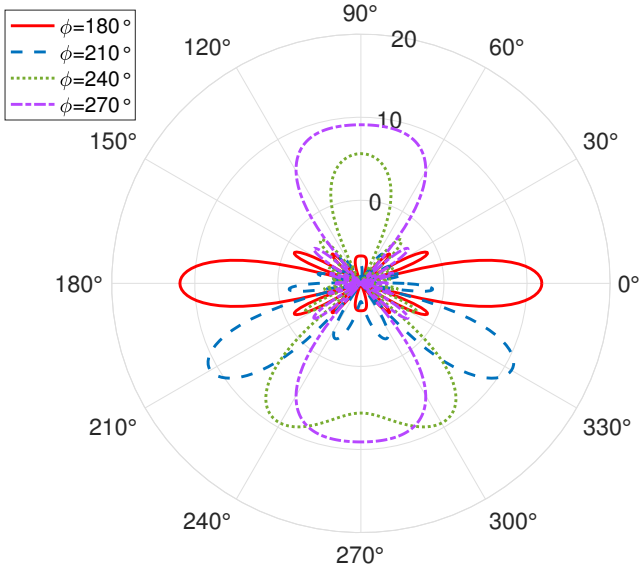


Fig. 8. Radiation pattern of a conventional ULA with  $N_A = 7$  active elements.

#### IV. NUMERICAL RESULTS

In this section, we present some numerical results related to the use cases described in Sec. III with the purpose of validating and investigating the potential of the DSA with respect to classical array structures and SIM. The following parameters have been considered in the numerical evaluations if not otherwise specified:  $f_0 = 2.4$  GHz,  $G_R = 0$  dB,  $R = 50$  Ohm, half-wavelength vertically oriented dipoles. Matrix  $\mathbf{Z}(f)$  has been computed analytically using the coupling model in [43]. Different and more complex implementations of antenna elements can be considered as well. In such cases,  $\mathbf{Z}(f)$  can be computed off-line using EM tools. In [25], examples using Hertzian dipoles are provided.

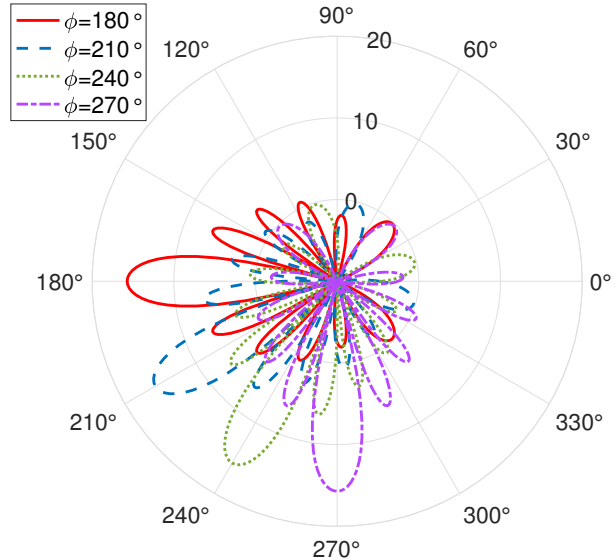


Fig. 9. Radiation pattern of a conventional UCA with  $N_A = 36$  active elements.

##### A. Model for the Reconfigurable Loads

Regarding the reconfigurable load, we consider a varactor diode whose equivalent circuit model is reported in Fig. 6, as suggested in [47]. By varying the polarization current of the diode (typically a few nA), its equivalent capacitance, and hence its impedance, can be changed. The corresponding impedance is

$$z(f; \theta) = \frac{j2\pi f L_1(j2\pi f L_2 + 1/(j2\pi f C(\theta)) + R_v)}{j2\pi f(L_1 + L_2) + 1/(j2\pi f C(\theta)) + R_v} \quad (35)$$

where  $C(\theta) = C_{\min} + (C_{\max} - C_{\min})(\tan^{-1}(\theta) + \pi/2)/\pi$ , being  $C_{\min}$  and  $C_{\max}$ , respectively, the minimum and maximum capacitance of the varactor. The relationship  $C(\theta)$  between the optimization parameters  $\theta$  and  $C$  is arbitrary but must be monotonic, and has been chosen so that  $\theta$  is unbounded and the optimization problem in (27) remains unconstrained, thus making its numerical solution computation faster. Varactor diodes exhibit minimal power consumption due to their negligible reverse leakage current so the power consumption of the DSA is determined by the digital control circuitry and the specific technology to realize it [48]. In the numerical results, the following parameters have been considered:  $R_v = 0.1$  Ohm,  $L_1 = 2.5$  nH,  $L_2 = 0.7$  nH,  $C_{\min} = 0.47$  pF,  $C_{\max} = 2.35$  pF [47].

##### B. Superdirective Beam Forming

We first investigate the single-frequency ( $K = 1$ ) beam forming capabilities of the DSA using one RF chain ( $N_A = 1$  active antenna element) and the deployment of the surrounding reconfigurable scatterers according to  $L_R$  vertical disks (along the  $z$ -axis) each of them composed of  $L$  concentric rings (layers) with incremental radius of step  $\Delta_R$  (see Fig. 3). This cylindrical structure appears particularly appealing, especially for its use in base stations or access points, thanks to its circular symmetry. When  $L_R = 1$ , the cylinder degenerates

into a disk. Obviously, other structures can be considered as well, depending on the specific application.

The target end-to-end channel matrix  $\mathbf{H}_1^{(\text{opt})} = \mathbf{H}^{(\text{opt})}$  with  $T = 120$  test points deployed on the  $x - y$  plane at distance  $d = 100$  m (far field) according to the use case in Sec. III-B was considered for 4 different steering angles,  $180^\circ$ ,  $210^\circ$ ,  $240^\circ$ , and  $270^\circ$ , respectively. Only the optimization Step 2 was performed with  $N_i = 1500$  iterations and setting  $W_{D_1} = 1$  (in this case,  $W_{D_1}$  is a scalar and no digital processing takes place).

In Fig. 7, the radiation diagrams for the 4 steering angles obtained with  $\Delta_R = \lambda/4$ ,  $L = 5$ ,  $L_R = 1$  (disk shape), corresponding to  $N_S = 121$  scatterers are shown. Perfect matching is considered. As can be observed, the directivity  $D$  of the DSA is independent of the angle and it is about 18.2 dB. In addition, limited back radiation is obtained without the need to insert a ground plane that would impede the steering in the angle range  $[90^\circ - 270^\circ]$ .

For comparison, we consider the same structure organized as a SIM with an impedance matrix having the structure as in (17). The achieved directivity is about 14 dB in all directions (not displayed in the figure), corresponding to a performance loss of about 4 dB with respect to the DSA. As pointed out in the Introduction, the performance of any SIM is constrained by the final layer of the structure, therefore it is upper bounded by that one can obtain by replacing the SIM with a fully digital architecture offering unrestricted processing flexibility followed by a planar or linear array with the same layout and number of elements of the final layer of the SIM. Therefore, for the sake of comparison, we consider the radiation diagrams obtained using a standard ideal full-digital ULA and a uniform circular array (UCA) with the same aperture of the DSA (36 cm diameter) in the  $x - y$  plane. The corresponding radiation diagrams are reported in Figs. 8 and 9, respectively. These arrays require  $N_A = 7$  and  $N_A = 36$  active antennas compared to only one active antenna of the DSA. As well-known, in ULAs the directivity degrades when approaching  $90^\circ$  from a maximum value of 11.7 dB (about  $10 \log_{10}(N_A G_d)$ , with  $G_d$  the directivity of the half-wave dipole) and symmetric back radiation is present. Instead, with the UCA, the directivity (15.7 dB) is insensitive to the steering direction at the expense of higher side lobes. Nevertheless, in both cases, the proposed DSA exhibits superdirective capability with an additional gain of 6.5 dB and 2.5 dB, respectively. Contrary to standard arrays, where superdirective is obtained only in the end-fire direction [49], here notably, superdirective is equally obtained in all steering directions. Superdirective cannot be obtained instead using a SIM-like structure.

In Tables I-III, the impact of the layers spacing  $\Delta_R$ , number of layers  $L$ , and the number of disks  $L_R$  is investigated. As it can be noticed in Table I, the maximum directivity is obtained for  $\Delta_R = \lambda/4$ , confirming that superdirective and a higher  $Q$  factor can be achieved only by exploiting the mutual coupling between the antenna elements but, at the same time, that there is an optimum spacing value to be found. In fact, on one hand, higher spacing reduces the coupling and hence the contribution to radiation of those scatterers located far away from the active element. On the other hand, very close spacing tightens the

TABLE I  
 $L_R = 1$ ,  $L = 5$ .

Configuration		Perfect matching			Simplified matching			
$\Delta_R$	$N_S$	$D$ (dB)	$\eta_d$	$Q$	$D$ (dB)	$\eta_m$	$\eta_d$	$Q$
$\lambda/8$	89	16.4	0.78	19.3	16	1	0.81	16.6
$\lambda/6$	100	17	0.8	19.4	17	1	0.82	15.7
$\lambda/4$	121	18.2	0.79	19.6	18.2	1	0.79	16.8
$\lambda/2$	184	15.6	0.82	4.82	15.7	0.92	0.92	4.3
$\lambda$	310	15.8	0.93	4.58	15	0.86	0.96	1.03

TABLE II  
 $L_R = 1$ ,  $\Delta_R = \lambda/4$ .

Configuration	$N_S$	$D$ (dB)	$\eta_m$	$\eta_d$	$Q$ -factor
$L = 3$	53	15.4	1	0.84	12.9
$L = 4$	84	16.4	1	0.82	15.7
$L = 5$	121	18.2	1	0.79	16.8
$L = 6$	174	19.1	1	0.78	17.6

coupling between the elements and reduces the DoF available for optimization. The impact of the dissipative elements on the efficiency  $\eta_d$  is more evident with close spacing between the elements (higher mutual coupling).

In Table I, the results for a DSA employing both the perfectly matched network and the simplified one proposed in Sec. II-B are reported. The comparison highlights a negligible difference in terms of directivity and that an almost perfect matching is reached in most of the configurations ( $\eta_m \approx 1$ ). Therefore, in the following results, only the simplified matching network is considered. A higher number of layers  $L$  (3D cylindrical structure) increases the directivity in the  $x - y$  plane at the expense of a higher number of reconfigurable scattering elements  $N_S$ , as reported in Table II. The directivity can be further increased by thinning the radiation diagram in the  $z$  direction by introducing more disks  $L_R$ , i.e., moving from a dish shape to a cylindrical shape, and it can be observed in Table III.

An example using a random deployment of the scatterers within a disk as a function of their density is provided in Table IV for a fixed diameter of 36 cm. As can be seen, the achievable performance is similar to that of the regular cylindrical deployment when compared with the same number of scatterers, even though, in general, higher values of  $Q$ -factor are obtained because of the possibility that a couple of scatterers are very close to each other. The analysis and optimization of the deployment strategies of the scatterers is a topic that deserves future investigations.

An interesting aspect worth consideration is the sensitivity of the performance to parameter mismatch that might arise in practical implementations. We evaluated the directivity degradation for the configuration in Fig. 7 when the actual implemented  $n$ th parameter of the DSA,  $\hat{\theta}_n$ , is affected by an error  $d_n$  modeled as a zero-mean Gaussian random variable with standard deviation  $\sigma_n$ , i.e.,  $\hat{\theta}_n = \theta_n + d_n$ . The corresponding directivity obtained for  $\sigma_n = 0$ ,  $\sigma_n = 10\%$  and  $\sigma_n = 20\%$  of the nominal absolute value  $|\theta_n|$  are, respectively,  $D = 18.2$  dB ( $\eta_m \approx 1$ ),  $D = 17.7$  dB ( $\eta_m = 0.86$ ), and  $D = 15.5$  dB ( $\eta_m = 0.85$ ), showcasing about 3 dB loss with

TABLE III  
 $L = 5, \Delta_R = \lambda/4$ .

Configuration	$D$ (dB)	$N_S$	$\eta_m$	$\eta_d$	$Q$ -factor
$L_R = 1$	121	18.2	1	0.79	16.8
$L_R = 2$	168	18.4	1	0.82	13.5
$L_R = 3$	252	19.4	0.98	0.79	14.3

TABLE IV  
RANDOM SHAPE.  $L_R = 1$

$N_S$	60	121	242	400
$D$ (dB)	16	17.8	19	19.5
$\eta_m$	0.97	1	1	
$\eta_d$	0.85	0.78	0.73	0.66
$Q$ -factor	10.71	16.5	21	26.3

20% relative error.

The capability of the DSA to provide frequency-selective radiation diagrams can be observed in Fig. 10, obtained with one RF chain and  $K = 4$  subcarriers distributed within the bandwidth  $W = 80$  MHz. The target steering angles for each subcarrier are:  $180^\circ, 210^\circ, 300^\circ$ , and  $330^\circ$ . Compared to the single-carrier situation, the diagrams present slightly lower directivities and higher sidelobes, indicating that managing wideband signals with the same configuration parameters of the DSA is more challenging. The motivation might be ascribed to the usage of dipoles with length equal to the wavelength at the carrier frequency  $f_0$ , whereas the actual used frequency differs from  $f_0$  for  $k > 1$ .

An example of multi-functional and multi-frequency design is reported in Fig. 11, where each RF chain ( $N_A = 2$  in this case) is associated with a different response for  $K = 2$  different frequencies. The target steering angles for each input/subcarrier (sc) combination are:  $180^\circ$  (input 1, sc 1),  $210^\circ$  (input 1, sc 2),  $300^\circ$  (input 2, sc 1), and  $330^\circ$  (input 2, sc 2). The plots show that with the same configuration  $\theta$ , obtained from the minimization of (22), the DSA is capable of associating a dedicated beam with each input/subcarrier combination. While the resulting diagrams demonstrate the interesting flexibility of DSA in providing flexible frequency-selective responses, the reduced gain indicates that the wideband design of DSA deserves further investigation, left to future works.

### C. Multi-user MISO

We consider now the scenario of use case 2 in Sec. III-C illustrated in Fig. 4, where a DSA with  $\Delta_R = \lambda/4$ ,  $L_R = 1$ ,  $N_A = 4$  active antennas and  $N_A$  RF chains is used to communicate simultaneously with  $T = N_A$  single-antenna users located at a distance of  $d = 100$  m and angles  $-40^\circ, 20^\circ, 80^\circ$ , and  $200^\circ$  in the  $x - y$  plane. The DSA has been optimized according to (28) (zero forcing criterium) with  $N_i = 50$  and  $N_{\text{alt}} = 10$ .

The corresponding performance is shown in Fig. 12, where the sum spectral efficiency (SE) is plotted as a function of the power  $\sigma^2$  of the AWGN for a transmitted power  $P_T = 10$  mW and for different numbers of layers  $L$ . The results obtained

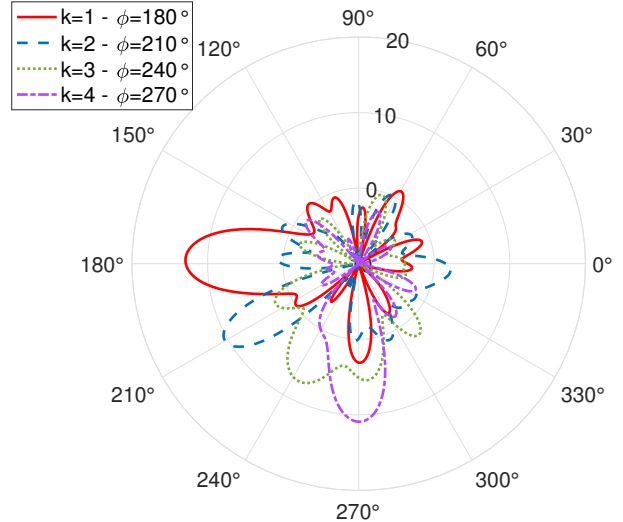


Fig. 10. Multi-frequency radiation diagrams of a disk-shaped DSA with  $\Delta_R = \lambda/4$ ,  $L = 5$ ,  $N_A = 1$ ,  $K = 4$  subcarriers, and  $W = 80$  MHz.

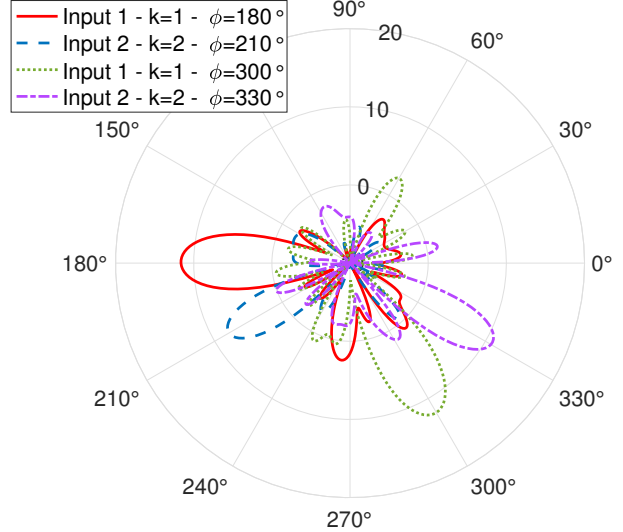


Fig. 11. Multi-frequency multi-input radiation diagrams of a disk-shaped DSA with  $\Delta_R = \lambda/4$ ,  $L = 5$ ,  $N_A = 2$ ,  $K = 2$  subcarriers, and  $W = 80$  MHz.

with a SIM configuration employing the same geometry as well as with an ideal system with perfect zero forcing and directivity of  $D = 17$  dB are also reported for comparison. The presence of a saturation for small  $\sigma^2$ , i.e., higher signal-to-noise ratios (SNRs), reveals an imperfect nulling of the multi-user interference. The DSA showcases much higher sum SE corresponding to a better approximation of the zero forcing criterion than the SIM for the same geometry. In this setup, the DSA provides the best performance with  $L = 7$  layers, whereas the SIM exhibits a tradeoff whose optimum is  $L = 5$  layers.

### D. MIMO EM Precoder

Finally, we consider the scenario of use case 3 in Sec. III-D illustrated in Fig. 5, where a multi-layer MIMO link with a user located at  $d = 10$  m equipped with a standard ULA with 20 elements spaced of  $\lambda/2$  has to be established in

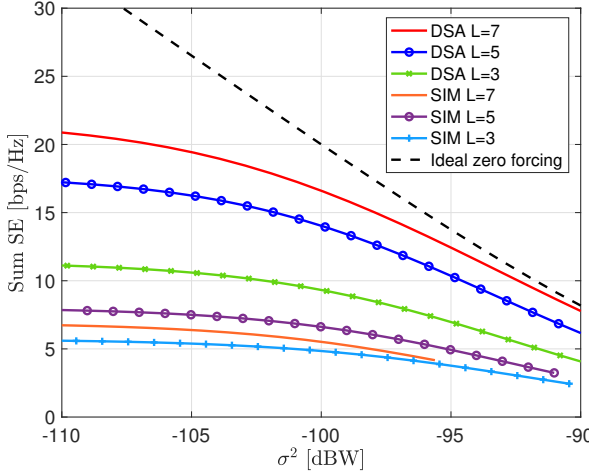


Fig. 12. Sum spectral efficiency of a zero-forcing 4-user MISO system based on a DSA and a SIM for different numbers of layers  $L$ .

non-line-of-sight (NLOS) condition. The DSA is equipped with  $N_A = 4$  active antennas and  $N_A$  RF chains to allow the transmission of up to 4 data streams (layers) according to channel characteristics. The simulated NLOS channel consists of 5 multi-paths caused by the reflection of 5 scatterers located at angles  $\phi = \{-43^\circ, -14^\circ, 14^\circ, 43^\circ, 72^\circ\}$  and distance 5 m from the DSA. The corresponding strongest singular values of the channel are  $\Lambda = \text{diag}(-37.3 \text{ dB}, -39.8 \text{ dB}, -42 \text{ dB}, -48.8 \text{ dB}, -82 \text{ dB}, \dots)$ , which has clearly rank  $r = 4$ . The DSA has the following parameters  $\Delta_R = \lambda/4$ ,  $L_R = 1$ ,  $N_S = 121$ , and it is optimized according to the criterium in (31) with  $N_i = 50$  and  $N_{\text{alt}} = 10$ .

In Table V, the resulting coefficients  $\hat{\Lambda}$  of the end-to-end channel are reported. The comparison between the diagonal and off-diagonal values indicates that the coupling between different layers is completely negligible, i.e., the channel is almost perfectly diagonalized. Compared to the singular values of the channel in  $\Lambda$ , the diagonal elements of  $\hat{\Lambda}$  exhibit the same behavior with a loss of about  $7 - 8$  dB that can be ascribed to the fact that the DSA is not ideal. The effect of implementation errors is reported in the bottom part of the table for 1% and 10% relative error standard deviation, respectively. It can be seen that the effect of implementation errors becomes no longer negligible (coupling above  $-10$  dB) with 10% relative error. In addition, numerical investigations revealed that the presence of the digital processor is not fundamental from the performance viewpoint, but slightly speeds up the convergence of the optimization process.

## V. CONCLUSION

In this paper, we have presented a general framework for the characterization and optimization of frequency-selective dynamic scattering arrays (DSAs). This has been achieved through an accurate modeling of the coupling between the scattering elements and their loads, and the joint optimization of EM processing, power matching, and radiation of the active and reconfigurable scattering elements interacting in

TABLE V  
[ $\hat{\Lambda}$ ] <sub>$n,k$</sub>  IN DB, FOR  $n, k = 1, 2, 3, 4$ .

Perfect implementation			
-45.2	-184	-186	-175
-175	-48	-190	-177
-182	-183	-49.8	-174
-172	-174	-165	-56.7
1% relative implementation error			
-45.6	-67	-81	-74
-69	-47.3	-86	-75
-68	-78	-49.6	-71
-75	-84	-99	-57
10% relative implementation error			
-43.5	-57	-56	-59
-66.6	-48	-55	-60
-68	-67	-51	-69
-71	-66	-70	-54

the reactive near field. It has been shown that a SIM can be modeled as a particular case of a DSA and that, for a given geometry, the DSA outperforms SIM in approximating the desired processing and enables the exploitation of superdirective capabilities.

The results obtained in this paper demonstrate the potential of DSA to realize multifunctional and multi-frequency processing tasks “over the air” by leveraging the coupling between active and scattering elements, thus minimizing the number of RF chains and baseband processing in the digital domain. This is achieved through a semi-passive structure with minimal energy consumption and nearly zero latency, as the processing occurs at the speed of light.

## ACKNOWLEDGMENT

This work was supported by the European Union under the Italian National Recovery and Resilience Plan (NRRP) of NextGeneration EU, partnership on “Telecommunications of the Future” (PE00000001 - program “RESTART”), by the HORIZON-JU-SNS-2022-STREAM-B-01-03 6G-SHINE project (Grant Agreement No. 101095738), and by the HORIZON-JU-SNS-2022 project TIMES (Grant no. 101096307).

## REFERENCES

- [1] A. Dang, S., B. O., Shihada, and et al., “What should 6G be?” *Nature Electronics* 3, vol. 20-29, 2020.
- [2] N. Gonzalez-Prelcic, M. Furkan Keskin, O. Kaltiokallio, M. Valkama, D. Dardari, X. Shen, Y. Shen, M. Bayraktar, and H. Wymeersch, “The integrated sensing and communication revolution for 6G: Vision, techniques, and applications,” *Proceedings of the IEEE*, vol. 112, no. 7, pp. 676–723, July 2024.
- [3] E. Björnson, L. Sanguinetti, H. Wymeersch, J. Hoydis, and T. L. Marzetta, “Massive MIMO is a reality - what is next?: Five promising research directions for antenna arrays,” *Digital Signal Processing*, 2019. [Online]. Available: <http://www.sciencedirect.com/science/article/pii/S1051200419300776>
- [4] D. Dardari and N. Decarli, “Holographic communication using intelligent surfaces,” *IEEE Communications Magazine*, vol. 59, no. 6, pp. 35–41, June 2021.
- [5] E. Björnson, Y. C. Eldar, E. G. Larsson, A. Lozano, and H. V. Poor, “Twenty-five years of signal processing advances for multiantenna communications: From theory to mainstream technology,” *IEEE Signal Processing Magazine*, vol. 40, no. 4, pp. 107–117, 2023.

- [6] C. You, Y. Cai, Y. Liu, M. D. Renzo, T. M. Duman, A. Yener, and A. Lee Swindlehurst, "Next generation advanced transceiver technologies for 6G and beyond," *IEEE Journal on Selected Areas in Communications*, pp. 1–1, 2025.
- [7] M. R. Castellanos, S. Yang, C.-B. Chae, and R. W. Heath, "Embracing reconfigurable antennas in the tri-hybrid MIMO architecture for 6G," 2025. [Online]. Available: <https://arxiv.org/abs/2501.16610>
- [8] Z. Wang, J. Zhang, H. Du, W. E. I. Sha, B. Ai, D. Niyato, and M. Debbah, "Extremely large-scale MIMO: Fundamentals, challenges, solutions, and future directions," *IEEE Wireless Communications*, pp. 1–9, 2023.
- [9] S. Phang, M. T. Ivrla, G. Gradoni, S. C. Creagh, G. Tanner, and J. A. Nossek, "Near-field MIMO communication links," *IEEE Transactions on Circuits and Systems I: Regular Papers*, vol. 65, no. 9, pp. 3027–3036, 2018.
- [10] N. Decarli and D. Dardari, "Communication modes with large intelligent surfaces in the near field," *IEEE Access*, vol. 9, pp. 165 648–165 666, 2021.
- [11] Y. Liu, J. Xu, Z. Wang, X. Mu, and L. Hanzo, "Near-Field Communications: What Will Be Different?" *arXiv e-prints*, p. arXiv:2303.04003, Mar. 2023.
- [12] H. Zhang, N. Shlezinger, F. Guidi, D. Dardari, M. F. Imani, and Y. C. Eldar, "Beam focusing for near-field multiuser MIMO communications," *IEEE Transactions on Wireless Communications*, vol. 21, no. 9, pp. 7476–7490, Sep. 2022.
- [13] H. Zhang, N. Shlezinger, F. Guidi, D. Dardari, and Y. C. Eldar, "6G wireless communications: From far-field beam steering to near-field beam focusing," *IEEE Communications Magazine*, vol. 61, no. 4, pp. 72–77, April 2023.
- [14] G. Torcolacci, N. Decarli, and D. Dardari, "Holographic MIMO communications exploiting the orbital angular momentum," *IEEE Open Journal of the Communications Society*, vol. 4, pp. 1452–1469, 2023.
- [15] A. Alkhateeb, O. El Ayach, G. Leus, and R. W. Heath, "Channel estimation and hybrid precoding for millimeter wave cellular systems," *IEEE Journal of Selected Topics in Signal Processing*, vol. 8, no. 5, pp. 831–846, 2014.
- [16] D. Dardari, G. Torcolacci, G. Pasolini, and N. Decarli, "An Overview on Over-the-air Electromagnetic Signal Processing," *arXiv e-prints*, p. arXiv:2412.14968, Dec. 2024, under revision on IEEE Signal Proc. Magazine.
- [17] J. Zhu, Z. Wan, L. Dai, M. Debbah, and H. V. Poor, "Electromagnetic Information Theory: Fundamentals, Modeling, Applications, and Open Problems," *arXiv e-prints*, p. arXiv:2212.02882, Dec. 2022.
- [18] M. D. Renzo and M. D. Migliore, "Electromagnetic signal and information theory," *IEEE BITS the Information Theory Magazine*, pp. 1–13, 2024.
- [19] E. Björnson, C.-B. Chae, J. Heath, Robert W., T. L. Marzetta, A. Mezghani, L. Sanguinetti, F. Rusek, M. R. Castellanos, D. Jun, and Ö. Tufge Demir, "Towards 6G MIMO: Massive Spatial Multiplexing, Dense Arrays, and Interplay Between Electromagnetics and Processing," *arXiv e-prints*, p. arXiv:2401.02844, Jan. 2024.
- [20] D. Dardari, "Reconfigurable electromagnetic environments: A general framework," *IEEE Journal on Selected Areas in Communications*, vol. 42, no. 6, pp. 1479–1493, June 2024.
- [21] A. Silva, F. Monticone, G. Castaldi, V. Galdi, A. Alù, and N. Engheta, "Performing mathematical operations with metamaterials," *Science*, vol. 343, no. 6167, pp. 160–163, 2014. [Online]. Available: <https://science.sciencemag.org/content/343/6167/160>
- [22] J. An, C. Xu, D. W. K. Ng, G. C. Alexandropoulos, C. Huang, C. Yuen, and L. Hanzo, "Stacked intelligent metasurfaces for efficient holographic MIMO communications in 6G," *IEEE Journal on Selected Areas in Communications*, vol. 41, no. 8, pp. 2380–2396, 2023.
- [23] T. Gong, P. Gavriilidis, R. Ji, C. Huang, G. C. Alexandropoulos, L. Wei, Z. Zhang, M. Debbah, H. V. Poor, and C. Yuen, "Holographic MIMO communications: Theoretical foundations, enabling technologies, and future directions," *IEEE Communications Surveys & Tutorials*, vol. 26, no. 1, pp. 196–257, 2024.
- [24] D. Dardari, "3D electromagnetic signal processing," in *Proc. Asilomar Conf. on Signals, Systems and Computers*, Oct 2024.
- [25] D. Dardari, "Dynamic Scattering Arrays for Simultaneous Electromagnetic Processing and Radiation in Holographic MIMO Systems," *arXiv e-prints*, p. arXiv:2405.16174, May 2024.
- [26] R. Harrington, "Reactively controlled directive arrays," *IEEE Trans. Antennas Propag.*, vol. 26, no. 3, pp. 390–395, May 1978.
- [27] A. Kalis, A. G. Kanatas, and C. B. Papadias, *Parasitic Antenna Arrays for Wireless MIMO Systems*. Springer New York, NY, 2013.
- [28] D. Pozar, "Beam transmission of ultra short waves: An introduction to the classic paper by H. Yagi," *Proceedings of the IEEE*, vol. 85, no. 11, pp. 1857–1863, 1997.
- [29] G. C. Alexandropoulos, V. I. Barousis, and C. B. Papadias, "Precoding for multiuser MIMO systems with single-fed parasitic antenna arrays," in *2014 IEEE Global Communications Conference*, 2014, pp. 3897–3902.
- [30] J. C. Bucheli Garcia, M. Kamoun, and A. Sibille, "Low-complexity adaptive spatial processing of ESPAR antenna systems," *IEEE Trans. Wireless Commun.*, vol. 19, no. 6, pp. 3700–3711, Feb. 2020.
- [31] M. Faenzi, G. Minatti, D. González-Ovejero, F. Caminita, E. Martini, C. D. Giovampaola, and S. Maci, "Metasurface antennas: New models, applications and realizations," *Scientific Reports*, vol. 9, no. 10178, pp. 1–14, 2019.
- [32] N. Shlezinger, G. C. Alexandropoulos, M. F. Imani, Y. C. Eldar, and D. R. Smith, "Dynamic metasurface antennas for 6G extreme massive MIMO communications," *IEEE Wireless Communications*, vol. 28, no. 2, pp. 106–113, 2021.
- [33] K.-K. Wong, W. K. New, X. Hao, K.-F. Tong, and C.-B. Chae, "Fluid antenna system - Part I: Preliminaries," *IEEE Communications Letters*, vol. 27, no. 8, pp. 1919–1923, 2023.
- [34] L. Pringle, P. Harms, S. Blalock, G. Kiesel, E. Kuster, P. Friederich, R. Prado, J. Morris, and G. Smith, "A reconfigurable aperture antenna based on switched links between electrically small metallic patches," *IEEE Transactions on Antennas and Propagation*, vol. 52, no. 6, pp. 1434–1445, 2004.
- [35] D. Rodrigo, B. A. Cetiner, and L. Jofre, "Frequency, radiation pattern and polarization reconfigurable antenna using a parasitic pixel layer," *IEEE Transactions on Antennas and Propagation*, vol. 62, no. 6, pp. 3422–3427, 2014.
- [36] N. U. Hassan, J. An, M. Di Renzo, M. Debbah, and C. Yuen, "Efficient beamforming and radiation pattern control using stacked intelligent metasurfaces," *IEEE Open Journal of the Communications Society*, vol. 5, pp. 599–611, 2024.
- [37] J. An, M. Di Renzo, M. Debbah, H. V. Poor, and C. Yuen, "Stacked Intelligent Metasurfaces for Multiuser Downlink Beamforming in the Wave Domain," *arXiv e-prints*, p. arXiv:2309.02687, Sep. 2023.
- [38] J. An, C. Yuen, Y. L. Guan, M. D. Renzo, M. Debbah, H. V. Poor, and L. Hanzo, "Two-dimensional direction-of-arrival estimation using stacked intelligent metasurfaces," *IEEE Journal on Selected Areas in Communications*, vol. 42, no. 10, pp. 2786–2802, 2024.
- [39] C. Liu, L. Ma, Q. Z.J., and et al., "Classification of metal handwritten digits based on microwave diffractive deep neural network," *Nat Electron*, no. 5, pp. 113–122, 2022.
- [40] Z. Gu, Q. Ma, X. Gao, J. W. You, and T. J. Cui, "Classification of metal handwritten digits based on microwave diffractive deep neural network," *Advanced Optical Materials*, vol. 12, no. 7, p. 2301938, 2024. [Online]. Available: <https://onlinelibrary.wiley.com/doi/abs/10.1002/adom.202301938>
- [41] M. T. Ivrlac and J. A. Nossek, "Toward a circuit theory of communication," *IEEE Transactions on Circuits and Systems I: Regular Papers*, vol. 57, no. 7, pp. 1663–1683, 2010.
- [42] L. Han, H. Yin, and T. L. Marzetta, "Coupling matrix-based beamforming for superdirective antenna arrays," in *ICC 2022 - IEEE International Conference on Communications*, 2022, pp. 5159–5164.
- [43] C. A. Balanis, *Antenna Theory: Analysis and Design*. New Jersey, USA: Wiley, 2016.
- [44] Alibakhshikenari, M. Virdee, P. B.S. Shukla, and et al., "Improved adaptive impedance matching for RF front-end systems of wireless transceivers," *Sci Rep* 10, no. 14065, pp. 1–11, 2020.
- [45] R. Fletcher, *Practical Methods of Optimization - Vol. I*. John Wiley and Sons, 1980.
- [46] D. Tse and P. Viswanath, *Fundamentals of Wireless Communication*. New York, NY: Cambridge University Press, 2005.
- [47] S. Abeywickrama, R. Zhang, Q. Wu, and C. Yuen, "Intelligent reflecting surface: Practical phase shift model and beamforming optimization," *IEEE Transactions on Communications*, vol. 68, no. 9, pp. 5849–5863, 2020.
- [48] J. Rains, J. U. R. Kazim, A. Tukmanov, L. Zhang, Q. Abbasi, and M. Imran, "Fully-addressable varactor-based reflecting metasurface with dual-linear polarisation for low power reconfigurable intelligent surfaces," in *2023 17th European Conference on Antennas and Propagation (EuCAP)*, 2023, pp. 1–5.
- [49] M. T. Ivrlac and J. A. Nossek, "The multiport communication theory," *IEEE Circuits and Systems Magazine*, vol. 14, no. 3, pp. 27–44, 2014.